Journal of MATERIALS RESEARCH

Article
DOI:10.1557/s43578-022-00749-1

Bi_2WO_6/UiO-NH_2-66 heterojunction photocatalysts with enhanced visible light organic pollutants removal

Junnan Chen[1], Wensong Lin[1,a], Xin Mai[1], Qian Yang[1]

[1] School of Materials Engineering, Shanghai University of Engineering Science, Shanghai 201620, People's Republic of China

[a] Address all correspondence to this author. e-mail: wslin@sues.edu.cn

Received: 27 July 2022; accepted: 16 September 2022; published online: 28 September 2022

In this work, the flower-like hierarchical Bi_2WO_6 decorated with nano UiO-NH_2-66 was fabricated by a two-step solvothermal method. The structure, composition, and morphology of the composites were characterized by XRD, FTIR, XPS, BET, and SEM. The photoelectrochemical properties of the composites were analyzed by transient photocurrent response, DRS, and PL spectra. It is found that hole ($\cdot h^+$) plays a dominant role, and the hydroxyl radical ($\cdot OH$) and superoxide radical ($\cdot O_2^-$) play a secondary role in the catalytic system after free radical trapping experiments. The results of electron spin resonance spin-trapping tests also confirm the mechanism. Compared with pure Bi_2WO_6 or pure UiO-NH_2-66, Bi_2WO_6/UiO-NH_2-66 composites have much higher decomposition effectiveness of Rhodamine B under the same conditions. Furthermore, Bi_2WO_6/UiO-NH_2-66 photocatalyst with 7 wt% of UiO-NH_2-66 (denoted as BWO/UNH-7) kept the stable catalytic performance after five recycles, which may be used as a good photocatalyst for degrading organic matter in sewage.

Introduction

As a large amount of wastewater was discharged into the environment, water pollution is becoming a serious problem damaging the ecosystem and harming the human body [1]. As the ubiquitous pollution species in the dye wastewater, Rhodamine B (RhB) widely used in food and textiles industries causes serious damage to the eyes and subcutaneous tissue and need to be removed from sewage urgently by some efficient methods [2].

Compared with the conventional wastewater treatment via adsorption techniques, photocatalytic degradation is more environmentally friendly and economically advantageous [3]. In this way, organic pollutants can be decomposed into pollution-free substances, such as CO_2 and H_2O efficiently [4]. Therefore, photocatalytic degradation technology has attracted extensive attention in the field of environmental remediation. However, photocatalysts used today are still restricted by several drawbacks including a big forbidden band and easy recombination of the photogenerated electron–hole pairs, resulting in limited utilization of the visible light spectra and low quantum efficiency [5]. Therefore, it is important to manufacture efficient and stable photocatalysts for environmental protection. As a new non-toxic and high chemical stable semiconductor, Bi_2WO_6 with a narrow band gap has a great application potential in the field of photocatalysis [6]. However, the recombination rate of the photogenerated carriers produced by Bi_2WO_6 under illumination is pretty high. The construction of visible light heterojunctions is a more significant way to reduce the recombination rate of photogenerated carriers [7–11]. Li et al. [12] built up a new S-scheme heterojunction photocatalysts with superior redox ability, by integrating $Cd_{0.5}Zn_{0.5}S$ nanoparticles on Bi_2WO_6 microspheres via a simple route. Huang et al. [13] found ways to promote the separation of photogenerated carriers by introducing oxygen vacancy and loading silver nanoparticles on Bi_2WO_6. Wang et al. [14] manufactured a kind of Bi_2WO_6 hybrid materials with carbon quantum dots to achieve the full spectral optical drive.

Metal–organic frameworks (MOFs) are substances with very high specific surface areas made from the connection of metal-containing nodes with organic ligands [15]. Due to their unique structure, MOFs have been widely used in gas storage, adsorption, sensor, H_2 production, and other aspects [16–21]. In general, due to the large band gap of the reported MOFs, photogenerated electrons can only be produced by MOFs under ultraviolet light, which limits their application in the field of photocatalysis. Compared with other MOFs, UiO-NH_2-66 has a higher visible light absorption capacity [22]. Therefore, the

loading of UiO-NH_2-66 on the surface of Bi_2WO_6 is used to improve the use of visible light by Bi_2WO_6 and the heterogeneous structure will lead to a substantial increase in the photocatalytic efficiency of the photocatalyst.

In this work, Bi_2WO_6/UiO-NH_2-66 (BWO/UNH) composites with type II heterojunction were synthesized by a two-step solvothermal method, by which Bi_2WO_6 nanoflowers is combined with trace nano UiO-NH_2-66. The structure, morphology, and optical properties of BWO/UNH composites were characterized by XRD, FTIR, SEM, BET, XPS, DRS, PL, and photoelectrochemical methods. The photocatalytic performance of the materials was tested by degrading RhB (20 mg/L) under visible light irradiation (> 420 nm). The results showed that BWO/UNH-7, the content of UNH in which is 7 wt%, got the highest degradation rate in all composites after two hours of illumination. Compared with pure BWO, the photocatalytic performance of composite was greatly improved. The photocatalytic active species of BWO/UNH-7 composite was investigated by ESR and free radical scavenging experiments, and the possible photocatalytic mechanism was proposed.

Results and discussion

XRD analysis

XRD patterns of the samples are shown in Fig. 1. The major diffraction peaks of UNH are found to be consistent with the report in references [23], so it can be concluded that UNH was successfully prepared in the experiment. The diffraction peaks in 2θ degrees of 28.299°, 32.790°, 47.138°, and 55.990° are consistent with the PDF card (JCPDS No. 39-0256), corresponding to the (131), (200), (202), and (133) crystal planes of BWO. The diffraction intensity of BWO implies that the material is finely crystalline. However, no diffraction peak of UNH in the XRD pattern of BWO/UNH-7 is found in Fig. S1, which is attributed to the low diffraction intensity of UNH in the BWO/UNH-7 [24]. To demonstrate that BWO/UNH-*x* composites have been synthesized successfully, other methods, as described below, were used to characterize the composites. In order to determine the ratio between BWO and UNH in BWO/UNH composites, the contents of Bi and Zr in BWO/UNH-7 were measured by ICPOES, which is shown in Table S1. As the contents of Bi and Zr in BWO/UNH-7 were 66.01% and 2.26%, respectively, we can calculate that the weight ratio between BWO and UNH in BWO/UNH-7 was 100:6.6. The result is quite consistent with the ratio of raw materials (100:7).

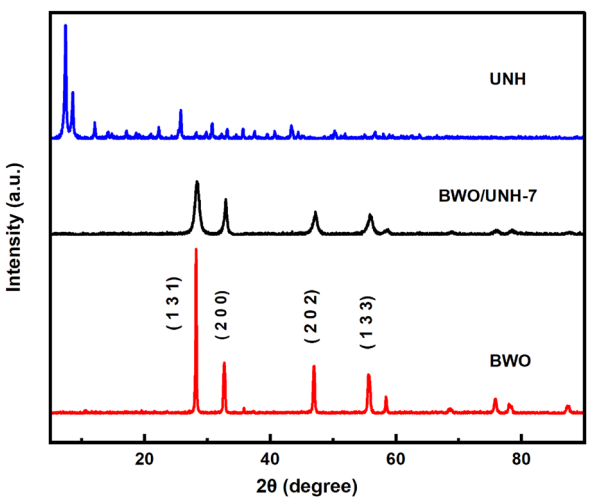

Figure 1: XRD patterns of BWO, UNH, and BWO/UNH-7.

SEM analysis

The morphologies of BWO, UNH, and BWO/UNH-7 were investigated by SEM. As shown in Fig. 2(a), the morphology of BWO is a flower-like microsphere structure composed of self-assembled nanosheets. Compared with stacked BWO nanosheets, the flower-like microsphere structure increases the direct void space of BWO nanosheets and improves the contact area between the material and the target pollutant [25]. Figure 2(b) shows that the morphology of pure UNH is spherical particles with a size of 70–80 nm. The morphology of BWO/UNH-7 composite is shown in Fig. 2(c) and (d) revealing that the UNH is decorated on the surface of the BWO in the composite and retains the original structure of BWO. The EDS mapping of BWO/UNH-7 composite [Fig. 2(e)] confirms that the elements Bi, W, O, Zr, N, and C are distributed in the composite, so it can be concluded that the combination of BWO and UNH is successful. It is believed that the composite is conducive to electron–hole transfer in the catalyst [26].

XPS analysis

XPS is used to analyze the elemental composition and valence states of materials. After charge correction of the data by C1s peaks, the typical peaks of Bi, O, W, N, C, and Zr are found in the X-ray diffraction energy spectrum of BWO/UNH-7 [Fig. 3(a)], which are in accord with the results of EDS stated above. The peaks of 37.5 eV and 35.4 eV in Fig. 3(b), which are ascribed to the W $4f_{5/2}$ and W $4f_{7/2}$ in BWO/UNH-7, respectively, are the convincing evidences of the existence of W^{6+}. The peaks near 159.1 eV and 164.4 eV [Fig. 3(c)] are attributed to Bi $4f_{5/2}$ and Bi $4f_{7/2}$, indicating the existence of Bi^{3+} [27]. It is well known that the offset of binding energy can reflect the variation of surface charge density, in which a rise in the binding energy signifies the reduced electron density and vice versa [28]. Compared with BWO, the peaks of Bi $4f_{5/2}$, Bi $4f_{7/2}$, W $4f_{5/2}$, and W $4f_{7/2}$ in the BWO/UNH-7 composite shift to the higher values [Fig. 3(b), (c)],

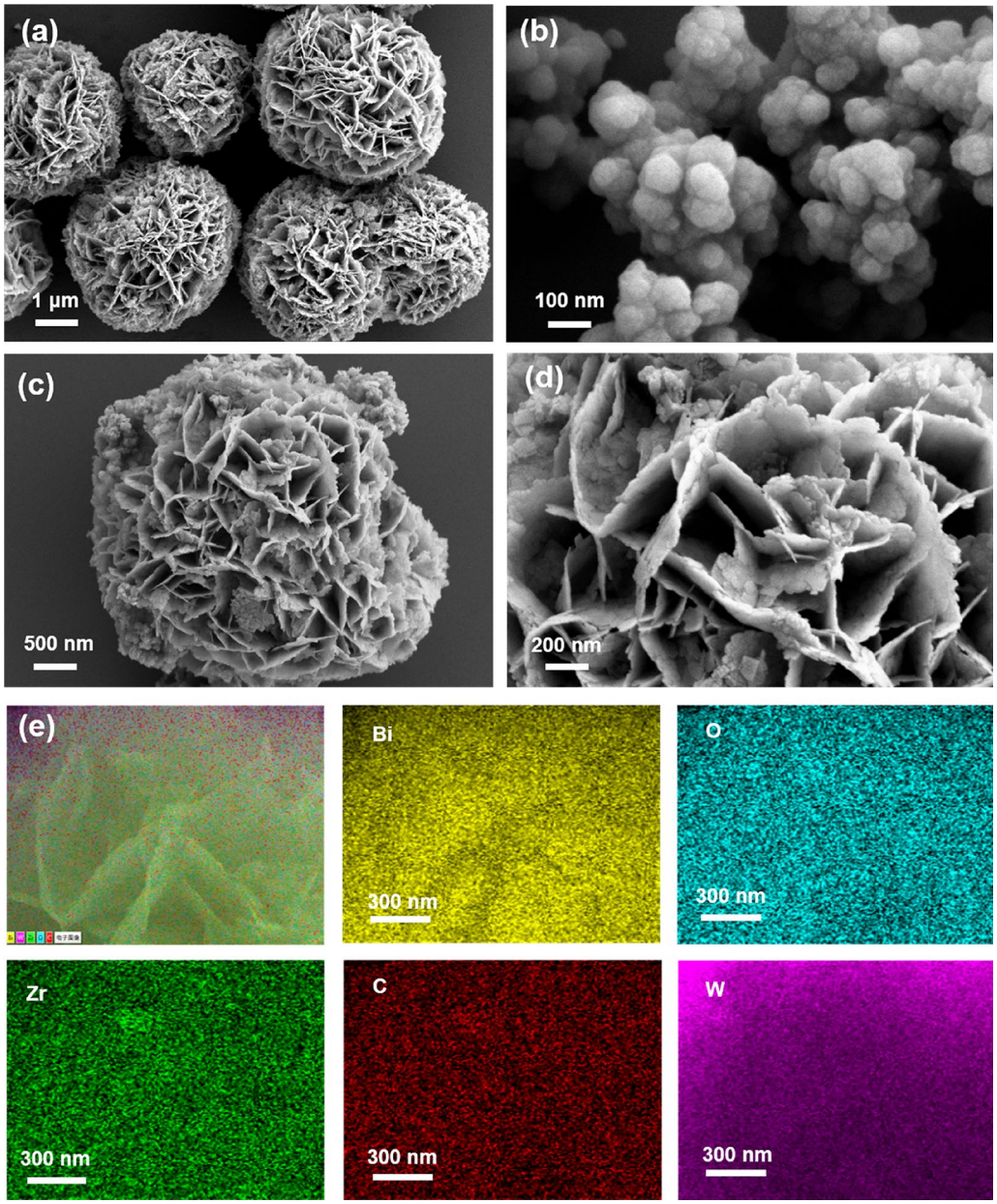

Figure 2: SEM morphologies of pure BWO (a), UNH (b), and BWO/UNH-7 (c, d); and EDS mapping of BWO/UNH-7 (e).

indicating that the photogenerated electrons on Bi and W are decreased in BWO/UNH-7. Therefore, it could be concluded that the electrons migrate from BWO to UNH on the BWO/UNH-7 interface, leading to the formation of the built-in electric field [24]. Similar evidence can be found in Fig. 3(d), in which peaks near 529.9, 530.7, and 531.7 eV in BWO, corresponding to Bi-O, W–O, and H–O, shift to 530.1, 531.5, and 532.7 eV in BWO/UNH-7, respectively, suggesting the existence of charge transfer between BWO and UNH in the composite [29]. As shown in Fig. 3(e), the peaks seated at 284.8 eV, 285.9 eV, and 288.2 eV are ascribed to C=C, C–C, and C=O in 2-NH_2-BDC [30]. In the composite, the binding energies near 182.6 eV and 184.9 eV are attributed to Zr $4d_{5/2}$ and Zr $4d_{3/2}$, which proves the existence of Zr^{4+} [Fig. 3(f)]. Due to the small content of Zr, the X-ray diffraction energy spectrum is not smooth enough [24]. The results of the X-ray diffraction energy spectrum provide another favorable evidence for the successful preparation of composite materials.

FTIR analysis

The groups and chemical bonds of as-prepared materials were analyzed by FTIR. As shown in Fig. S2, a series

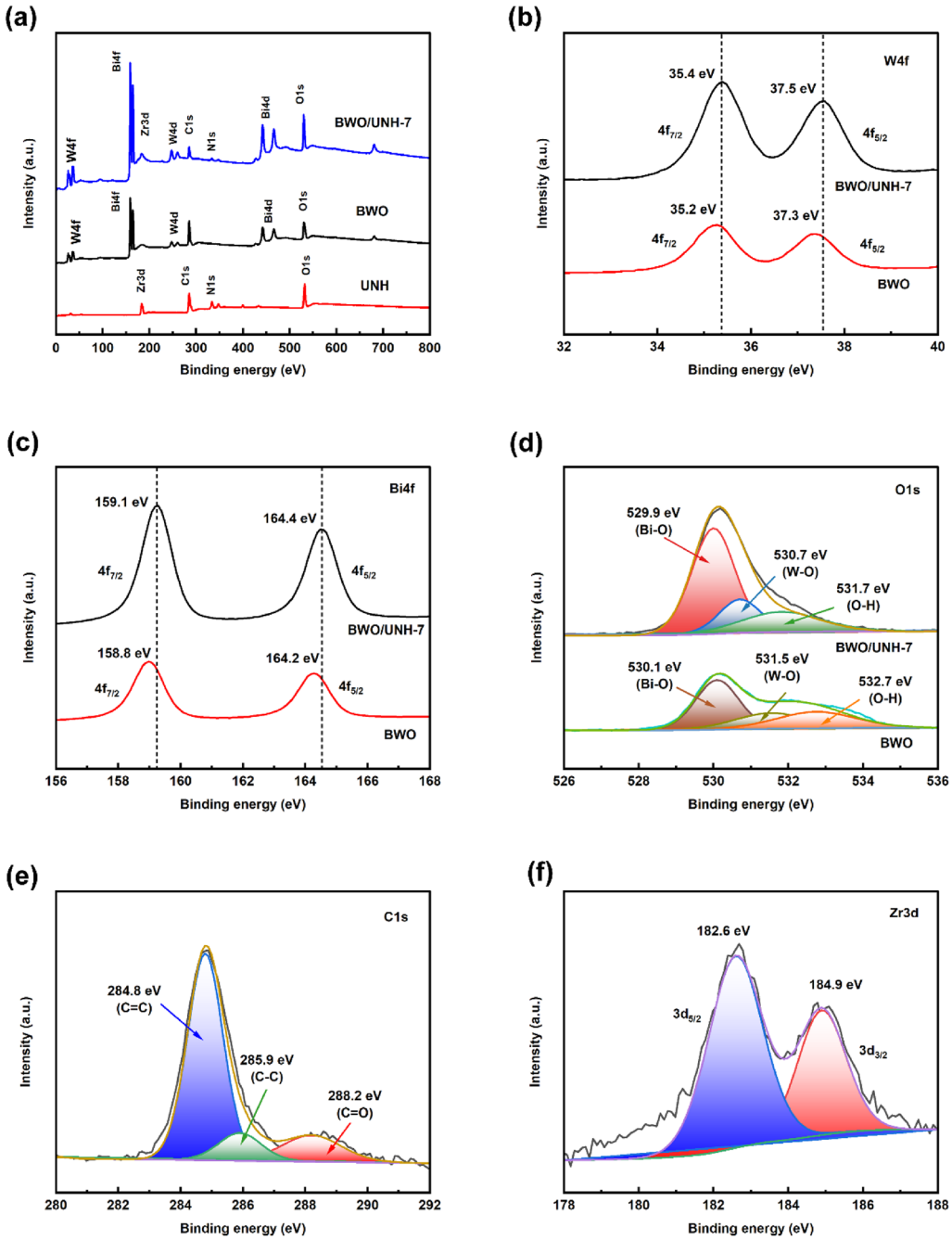

Figure 3: XPS spectra: (a) full spectra of BWO, UNH, and BWO/UNH-7; (b) W 4f of BWO and BWO/UNH-7; (c) Bi 4f of BWO and BWO/UNH-7; (d) O 1 s of BWO and BWO/UNH-7; (e) C 1 s of BWO/UNH-7; and (f) Zr 3d of BWO/UNH-7.

of characteristic peaks appeared at 768, 1258, 1655, and 1387 cm^{-1} in the absorption spectrum of as-prepared UNH are attributed to N–H wobble vibration, C–N stretching, asymmetric vibration of C=O, and stretching of carboxyl group in 2-NH_2-BDC ligand [31], respectively. The characteristic peak at 731 cm^{-1} of as-prepared BWO is due to asymmetric tensile vibration at W–O [24]. From Fig. S2, it can be also observed that all characteristic peaks of UNH and BWO in the absorption spectrum of BWO/UNH-7 and that peaks of BWO/UNH-7 are blue shifted slightly compared with BWO, indicating a certain interaction happened between BWO and UNH.

BET analysis

A typical type IV N_2 adsorption/desorption isotherms of the BWO, UNH, and BWO/UNH-7 are recorded in Fig. S3, in which the hysteresis loops can be seen in the curves at higher a relative pressure, so the characteristic mesoporous structure of BWO,

UNH, and BWO/UNH-7 is confirmed [32]. The surface areas of BWO, UNH, and BWO/UNH-7 are calculated to be 34.104 m^2/g, 860.201 m^2/g, and 36.501 m^2/g, respectively, by measuring N_2 adsorption–desorption isotherms (Fig. S3) [33]. Similarly, the pore volumes of BWO, UNH, and BWO/UNH-7 are calculated to be 0.103 cm^3/g, 0.463 cm^3/g, and 0.123 cm^3/g, respectively, by the Barrett–Joyner–Halenda desorption method [34]. The combination of UNH with BWO in BWO/UNH-*x* increases the surface area and pore volume of the composites, resulting in more adsorption sites and active sites to achieve the best photocatalytic performance.

Optical properties analysis

The photocatalytic activity of semiconductors is closely linked to their optical absorption properties and electronic structures. The UV–Visible diffusion absorption spectra of the as-prepared composites were obtained by UV spectrophotometer tests. As shown in Fig. 4(a), the absorption edge of pure BWO is at about 430 nm [35]. The strong absorption band of pure UNH is found from 300 to 450 nm [36]. The absorption edge of BWO/UNH-*x* has a red shift, so the light-harvesting capacity of the composite is improved and the photogenerated electron–hole pairs increase in the BWO/UNH materials [37].

In general, the Kubelka–Munk function (Formula 1) is used to calculate the bandgap width of the materials [38]:

$$\alpha h\nu = A\left(h\nu - E_g\right)^{n/2}, \tag{1}$$

where α, h, ν, and E_g represent absorption coefficient, Planck's constant, optical frequency, and band gap energy, respectively, A is a constant, and the value of the index n is related to the type of semiconductor [39]. Since BWO and UiO-NH_2-66 are indirect gap and direct gap semiconductors, their values of n are 4 and 1, respectively. According to formula 1, the BWO and UNH are estimated to have energy bandgaps of about 2.54 eV and 2.91 eV, respectively, as shown in Fig. 4(b) and (c).

The position of the valence band (VB) of the material can be determined by the XPS valence band (VB) spectrum. As shown in Fig. 5(a) and (b), the valence bands of BWO and UNH are estimated to be 1.34 eV and 2.05 eV, respectively. Through formula 2, the calculated conduction band (CB) of the materials can be obtained. The conduction band of BWO is – 1.20 eV, and the conduction band of UNH is – 0.86 eV.

$$E_{CB} = E_{VB} - E_g. \tag{2}$$

The Mott–Schottky curve is used to analyze semiconductor type and flat band potential. From the Mott–Schottky plot [Fig. 5 (c) and (d)], the slope of the curve is positive, which indicates that BWO and UNH were N-type semiconductors. The flat band energy positions of BWO and UNH are – 1.44 eV and – 1.10 eV. According to the Nernst equation ($E_{NHE} = E_{SCE} + 0.244$) [40], the E_{CB} of BWO and UNH concerning ordinary hydrogen electrode (vs NHE) is calculated to be – 1.20 eV and – 0.86 eV, which is consistent with the calculation result of formula 3 [41].

The separation efficiency of photogenerated carriers in as-prepared material was analyzed by PL spectra excited a wavelength of 290 nm. As shown in Fig. 6(a), the PL spectra of BWO exhibits the high emission peaks at 475 nm, attributing to the serious charge recombination and the band edge transition. The emission peak of BWO/UNH-7 is much weaker than that of BWO and UNH, after coupling with UNH. This result confirms that the heterojunction between BWO and UNH is formed, which effectively enhanced the separation and transfer of electrons and holes [42].

The transient photocurrent responses of BWO, UNH and BWO/UNH-7 are analyzed by photocurrent tests, which exhibit in Fig. 6(b). Photogenerated electron–hole pairs of the semiconductors could be motivated by visible light and transferred from the VB to CB to generate photocurrent. Therefore, the transient photocurrent is believed to be a useful tool to assess separation efficiency of photoinduced carriers. Compared with BWO and UNH, the transient photocurrent responses of BWO/UNH-7 has a higher instantaneous

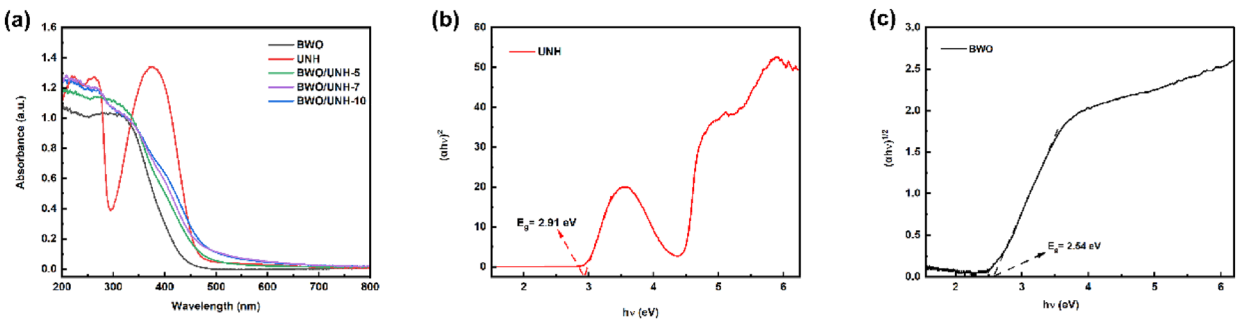

Figure 4: (a) UV–Vis DRS of BWO, UNH, BWO/UNH-5, BWO/UNH-7, and BWO/UNH-10, (b) plot of $(ahv)^2$-hv of UNH, and (c) plots of $(ahv)^{1/2}$-*hv* of BWO.

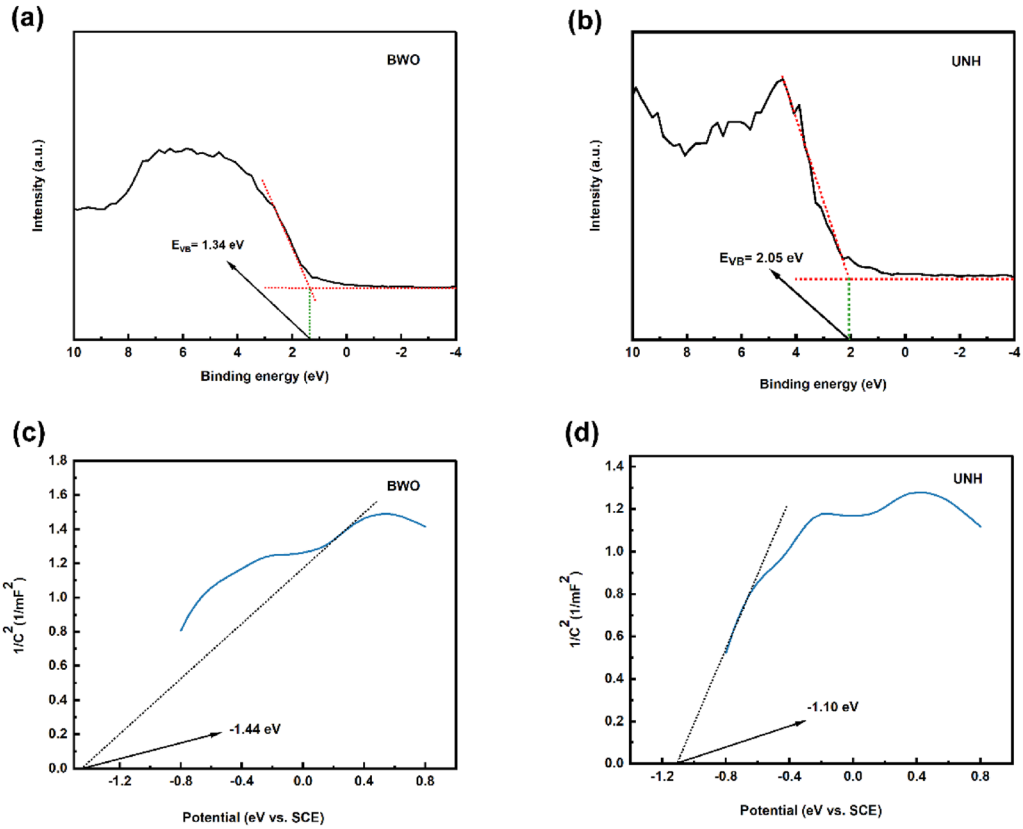

Figure 5: VB spectra of BWO (a) and UNH (b); M–S curves of BWO (c) and UNH (d).

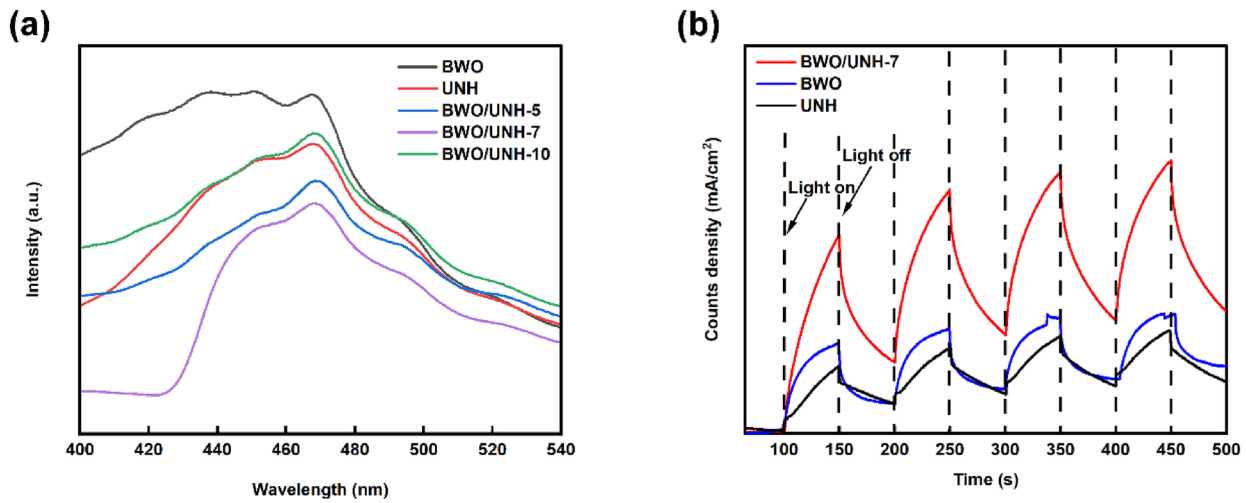

Figure 6: (a) Photoemission spectra (PL) of BWO, UNH, BWO/UNH-5, BWO/UNH-7, and BWO/UNH-10 at the excitation wavelength of 290 nm. (b) Transient photocurrent response curves of BWO, UNH, and BWO/UNH-7.

photocurrent response by light irradiation. The reason for this is the heterojunction of BWO/UNH-7 can achieve photoinduced electrons migration from CB of BWO to that of UNH, as well as transferring photoinduced holes from VB of UNH to that of BWO. Therefore, the recombination of photogenerated electron–hole pairs is suppressed and charge transfer is promoted, resulting in a higher photocurrent response. This is in accordance with the results of PL spectra.

Photocatalytic activity evaluation

The photocatalytic activities of the material were evaluated by photocatalytic degradation of RhB under Xe lamp irradiation ($\lambda > 420$ nm). As can be seen in Fig. 7, it is clear that RhB is hardly be decomposed under illumination without a catalyst. With the increase of irradiation time, the absorption band of RhB is blue shift, resulting from the diethyl reaction [30, 38]. It can still be seen from Fig. 7 that BWO/UNH-7 has a higher visible light degradation activity than BWO and UNH. The degradation rate of RhB by BWO, UNH, and BWO/UNH-7 are approximately 63.8%, 27.1%, and 93.1%, respectively. The excellent catalytic performance is assigned to the loading of UNH which increases the light absorption performance of the material, and the heterojunction structure between the two accelerates rapid photogenerated electron–hole pair separation. However, the photocatalytic performance of BWO/UNH was deteriorated if the weight ratio of UNH loaded on BWO exceeded 7 wt%, resulting from the shielding of the active sites as a result of the excess addition of UNH on the BWO [43].

Formula 3 is used to study the photocatalytic kinetics for the degradation of RhB.

$$-\mathrm{In}\left(\frac{C_t}{C_0}\right) = kt, \tag{3}$$

where C_0, C_t, and k represent the concentration of RhB at 0 and t minutes of illumination and the kinetic rate constant of the catalyst, respectively. As shown in Fig. 7(c), the plots of $(-\mathrm{In}(C_t/C_0))$ are linearly proportional to the reaction time. The average kinetic rate constants (k) of BWO/UNH-7, BWO, and UNH are 0.00819, 0.00543, and 0.00112 min^{-1}, respectively, so the k value of BWO/UNH-7 is 1.5 times and 7.3 times as more as that of BWO and UNH, respectively.

To determine the recycling potential of BWO/UNH-7, the five cycling experiments under the same reaction condition were tested. At the end of each cycle, the solutions were centrifuged to recover the used BWO/UNH-7. The BWO/UNH-7 used in the previous test cycle was washed with water and ethanol six times, followed by drying at 70 °C for 12 h before it was tested

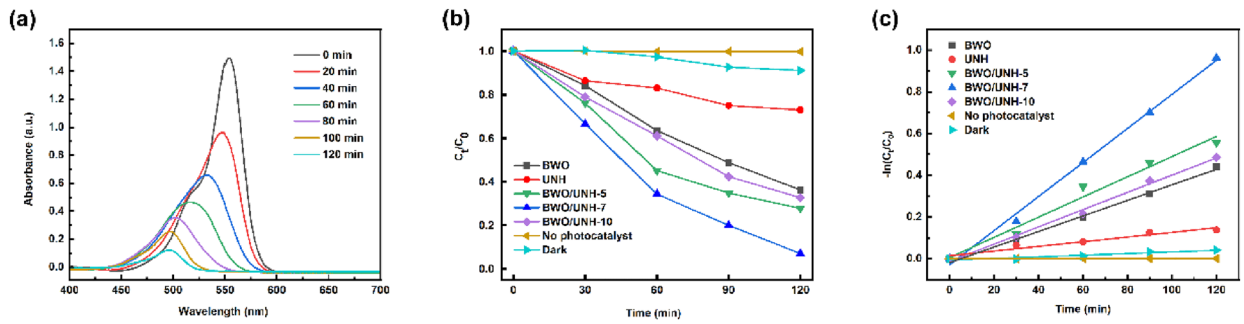

Figure 7: (a) UV–Vis absorption spectra of 20-mg/L RhB aqueous solution degraded by BWO/UNH-7, (b) degradation rates of RhB of the samples, and (c) k values of the first-order kinetic degradation rate of the samples.

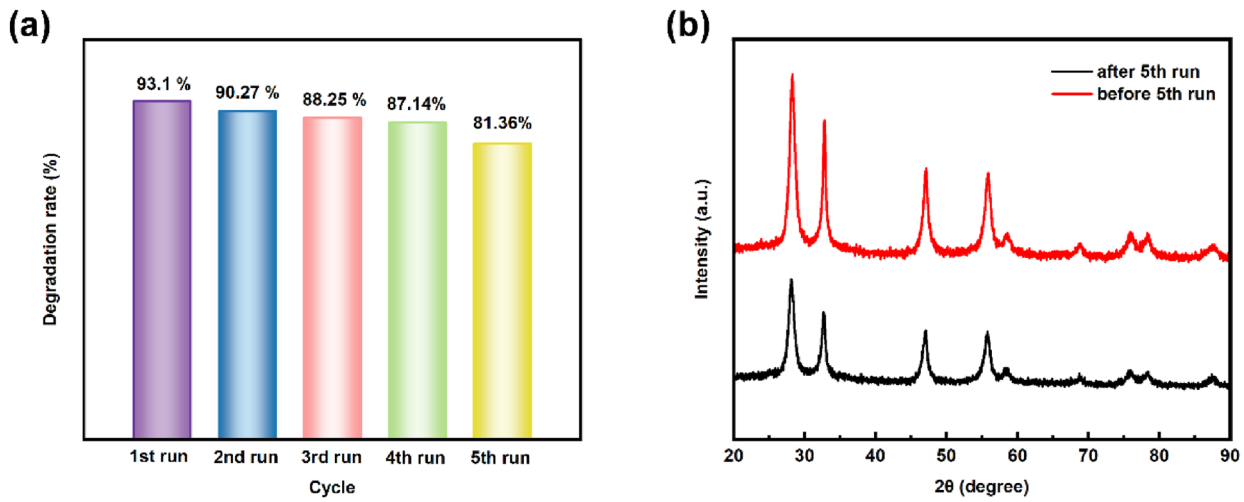

Figure 8: (a) The degradation rate of BWO/UNH-7 in five cycles and (b) XRD patterns of BWO/UNH-7 before and after used.

again in the next cycle. The test results are shown in Fig. 8(a), revealing that the degradation efficiency is about 81.36% on the fifth run. XRD was used to analyze the crystal structure of the BWO/UNH-7 composites before and after being tested in five cycles, which is shown in Fig. 8(b). The results clearly show that the crystalline of BWO/UNH-7 keeps stable after five-cycle tests. ICPOES experiments was used to determine the leaching of metal ions in photocatalyst after five-cycle tests, and the test results are shown in Table S1. It can be seen that the ratio between UNH and BWO in the photocatalyst keep the same value after five-cycle tests as before. The decrease in metal ion content may be due to, for example, slight leaching and the adsorption of undegraded RhB during cycling. Hence, the BWO/UNH-7 can be considered as an effective photocatalyst for RhB decomposition in practical applications.

Photocatalytic mechanism analysis

The reactive species of the BWO/UNH-7 in the photodegradation of RhB was analyzed by scavenger test. The isopropanol (IPA 1 mmol/L), p-benzoquinone (BQ 1 mmol/L), and EDTA-2Na (1 mmol/L) were used as trap agents to catch ·OH, $\cdot O_2^-$, and $\cdot h^+$, respectively. As can be seen from Fig. 9(a), the photocatalytic efficiency of BWO/UNH-7 decreases remarkably with the introduction of EDTA-2Na, as compared with isopropanol and para-benzoquinone. The results clearly show that holes are the foremost active species during photodegradation, but ·OH and $\cdot O_2^-$ radicals are insignificant active species in the reaction [44]. The electron spin resonance (ESR) test was used to further verify the reactive species in the photodegradation of RhB [45]. As shown in Fig. 9(b)–(d), the radical signal of ·OH, $\cdot O_2^-$, and $\cdot h^+$ are observed after 10 min of irradiation. There are the obvious signals of ·OH, $\cdot O_2^-$ and h^+ appeared after about 5 min of illumination. And after 10 min of illumination, the signals are all strengthened which further proved the existence of ·OH, $\cdot O_2^-$ and $\cdot h^+$ in the reaction. This result is consistent with the result of the scavenger test.

After summarizing the experimental results in this study, a tentative mechanism for the photodegradation of RhB by BWO/UNH-7 is proposed (Fig. 10). Based on the test results of UV–Vis DRS and Mott–Schottky, the energy bands of BWO and UNH are matched with each other which assigns to type II heterojunction. From Fig. 10, the BWO possesses a lower VB and higher CB position than UNH. The photo-excited hole may migrate from the VB of UNH to the VB of BWO, and the photoinduced electron may migrate from the CB of BWO to the CB of UNH. Therefore, the photogenerated electron–hole pairs can be separated effectively. The

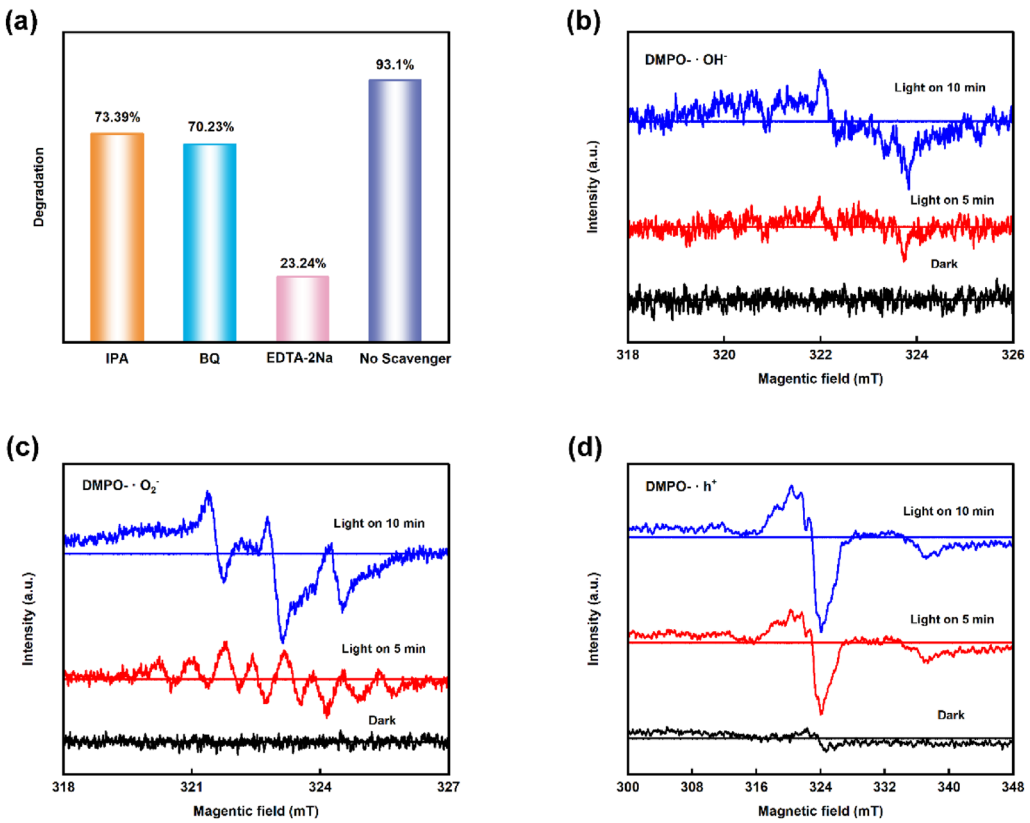

Figure 9: (a) Effects of different trapping agents on RhB degradation by BWO/UNH-7, (b) DMPO···OH, (c) DMPO···O_2^-, and (d) DMPO···h^+.

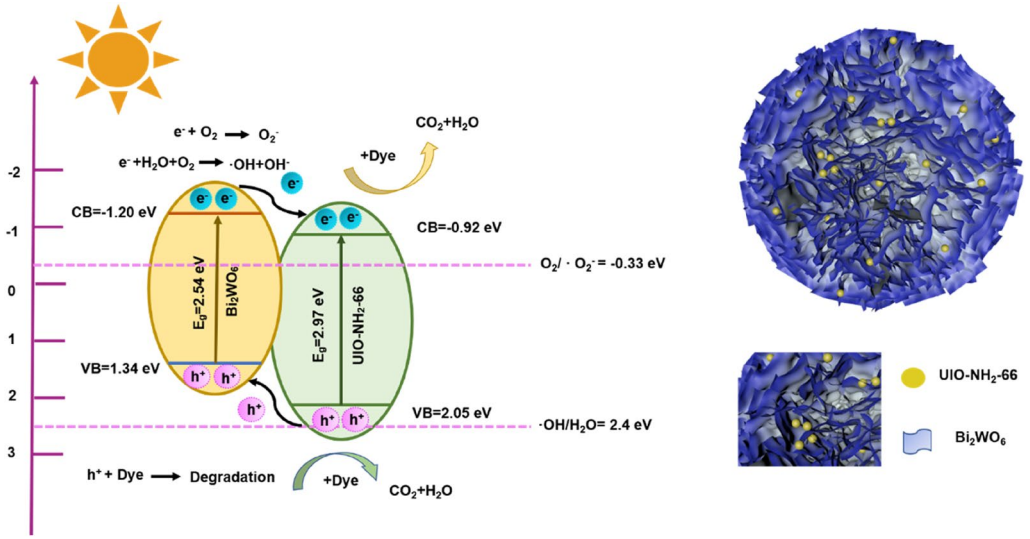

Figure 10: Photocatalytic degradation mechanism of RhB by BWO/UNH-7.

VB of BWO and UNH are more negative than the oxidation potential of $OH^-/\cdot OH$ (+ 2.40 eV), so the photoexcited hole cannot oxidize H_2O to ·OH. Due to the reduction potential of $O_2/\cdot O_2^-$ (-0.33 eV), the electrons on the CB of UNH generated $\cdot O_2^-$ and further converted to ·OH [28]. Therefore, h^+, $\cdot O_2^-$, and $\cdot OH^-$ are considered to be the reactive species for photodegradation of RhB in the process, which is matched to the scavenger and ESR test. Meanwhile, the surface area and pore volume of BWO/UNH-7 are larger than that of UNH or BWO, resulting in more adsorption sites and active sites exposed in the composite, so the degradation rate of RhB by the composite are much higher than that of UNH or BWO under the same tested condition.

Conclusion

BWO/UNH composites with II type heterojunction were synthesized through a two-step hydrothermal method. The specific surface area and photocatalytic active sites of the composites increase with the appropriate amount of UNH introduced onto the surface of the BWO. The degradation rate of RhB by BWO/UNH-7 reached 93.1% within 2 h, which was attributed to its wide absorption spectrum of visible light and low recombination rate of the photogenerated electron–hole pairs. After five cyclic experiments, the degradation capacity of BWO/UNH-7 remained at a high level. The tentative mechanism for the photodegradation of RhB by BWO/UNH-7 is proposed from the scavenger test and ESR investigation. It is found that hole ($\cdot h^+$) plays a dominant role, and the hydroxyl radical (·OH) and superoxide radical ($\cdot O_2^-$) play a secondary role in the catalytic system.

Experimental section

Materials

Bismuth nitrate pentahydrate ($Bi(NO_3)_3{\cdot}5H_2O$), sodium tungstate dihydrate ($Na_2WO_4{\cdot}2H_2O$), zirconium chloride ($ZrCl_4$), 2-aminoterephthalic acid (2-NH_2-BDC), N′N-dimethylformamide (DMF, $C_5H_{13}NO_2$), anhydrous methanol (CH_3OH), glacial acetic acid ($C_2H_4O_2$), and hydrochloric acid (HCl) were purchased from Aladdin Biotechnology Co., Ltd. (Shanghai, China). All the reagents used in the experiment were analytically pure and had not been further purified.

Preparation of composite materials

Preparation of Bi_2WO_6

Bi_2WO_6 was prepared by a hydrothermal method as we reported previously [46]. Briefly, 2.425 g $Bi(NO_3)_3{\cdot}5H_2O$ was dissolved in 10-mL glacial acetic acid and 1.639-g $Na_2WO_4{\cdot}2H_2O$ was dissolved in 90-mL deionized water. The two solutions were stirred and mixed together at room temperature for 1 h to form a homogeneous suspension. Then, the suspension was transferred to a polytetrafluoroethylene autoclave and maintained at 140 °C for 20 h. After cooling to room temperature, the powder was obtained by centrifugation. The powder was then washed with deionized water and dried overnight at 60 °C. The as-prepared powder (Bi_2WO_6) was indicated as BWO.

Preparation of UiO-NH_2-66

UiO-NH_2-66 was prepared by a similar hydrothermal method. In detail, 0.5-g $ZrCl_4$ was dissolved in 20-mL DMF and 4-mL HCl solution (called solution A). 0.5-g 2-NH_2-BDC was dissolved in 24-mL DMF (called solution B). Then, solution B was mixed with solution A and stirred for 10 min. The as-mixed uniform liquid was transferred to a polytetrafluoroethylene autoclave and maintained at 140 °C for 24 h. After cooling to room temperature, the powder was obtained by centrifugation, then washed with deionized water, and dried overnight at 60 °C. The as-prepared powder (UiO-NH_2-66) was denoted as UNH.

Preparation of Bi_2WO_6/UiO-NH_2-66 composites

Bi_2WO_6/UiO-NH_2-66 composites (BWO/UNH) were prepared by a simple solvent thermal mixing method. The as-prepared 0.2 g BWO was dispersed in 60-mL methanol and ultrasonicated for 5 min. Different masses of UNH powder were added to the above liquid to obtain a mixed solution of BWO/UNH with contents of 5, 7, and 10 wt% of UNH, respectively. The mixing solution was dispersed by sonication for 10 min, then transferred to a polytetrafluoroethylene autoclave, and maintained at 120 °C for 12 h. After cooling to room temperature, the powder was obtained by centrifugation, then washed with deionized water, and dried overnight at 60 °C. The as-prepared Bi_2WO_6/UiO-NH_2-66 composites with contents of 5, 7, and 10 wt% of UNH were indicated as BWO/UNH-x (x = 5, 7, 10).

Photocatalytic experiment

The photocatalytic activities of BWO/UNH-x were evaluated for degrading rhodamine B (RhB 20 mg/L) dye under Xe lamp irradiation (300 W, PLS SXE300C, Beijing Perfect Light Inc., China). About 20-mg photocatalytic BWO/UNH-x composites were dispersed in 40-ml rhodamine B solution (RhB, 20 mg/L) and stirred in darkness for 30 min to achieve adsorption–desorption equilibrium. Then the suspension was irradiated with a 300-W xenon lamp and stirred continuously. For every 30-min interval, 5 ml of the irradiated suspensions were centrifuged to eliminate the BWO/UNH-x photocatalysts, and the light absorbance of the residual supernatant was analyzed by UV–Vis spectrophotometer at 554 nm. Formula (4) is used to calculate the photocatalytic efficiency of the catalyst, where C_0 is the initial absorbance of RhB and C_t is the absorbance after the reaction.

$$\text{Degradation rate}(\%) = \left(1 - \frac{C_t}{C_0}\right) \times 100\%. \quad (4)$$

To study the photocatalytic stability for BWO/UNH-7 to remove RhB, cyclic experiments were carried out on the photocatalyst. The photocatalyst tested in the last cycle was collected, washed with deionized water, and then dried for 12 h at 60 °C. Thereafter, the dried photocatalyst was dispersed in a fresh solution with 20 mg/L of RhB for the next cycle of photodegradation under a similar experiment condition as stated above.

Characterization

The crystal structure of the photocatalysts was analyzed by X-ray diffractometry (Bruker D8 Advance). The morphology of the photocatalysts was observed by scanning electron microscopy (ZEISS Gemini 300). Fourier transform infrared spectra (FTIR) of the samples were obtained at 400–4000 cm^{-1} using an infrared spectroscopy analyzer (Thermo Scientific Nicolet iS5). X-ray diffraction spectroscopy (XPS) was performed on the Thermo Scientific K-Alpha instrument using Al Kα rays as excitation sources to determine the chemical state of the samples. $BaSO_4$ was used as the backing material to obtain the absorption spectrum of the photocatalytic material when measuring the UV–Vis diffuse reflectivity spectrum of the materials (Shimadzu UV 2600 DRS). The photoluminescence spectra (PL) of the photocatalyst were obtained on an F-7000 fluorescence spectrometer (excitation wavelength λ = 290 nm). The instantaneous photocurrent of the photocatalytic material was measured in 0.5-mol/L Na_2SO_4 solution on an electrochemical workstation (Chenhua Chi 660E), using a traditional three-electrode structure with Pt as a counter electrode and saturated calomel as a reference electrode.

Author contributions

JC performed the experiment and wrote the manuscript; WL contributed significantly to analysis and manuscript preparation; XM helped perform the analysis with constructive discussions; QY contributed to the conception of the study.

Funding

This work was funded by the National Natural Science Foundation of China: [Grant Number 81974317].

Data availability

All data generated or analyzed during this study are included in this published article.

Code availability

Not applicable.

Declarations

Conflict of interest The authors have no competing interests to declare that are relevant to the content of this article.

Supplementary Information

The online version contains supplementary material available at https://doi.org/10.1557/s43578-022-00749-1.

References

1. K. Xie, J. Fang, L. Li, J. Deng, F. Chen, Progress of graphite carbon nitride with different dimensions in the photocatalytic degradation of dyes: a review. J. Alloys Compd. **901**, 163589 (2022)
2. J. Zhang, M. Zhu, I. Jones, Z. Zhang, J. Gao, D. Zhang, Performance of activated carbons prepared from spent tyres in the adsorption of rhodamine B in aqueous solutions. Environ. Sci. Pollut. Res. **28**(38), 52862–52872 (2021)
3. B. Fang, Z. Xing, D. Sun, Z. Li, W. Zhou, Hollow semiconductor photocatalysts for solar energy conversion. Adv. Powder Mater. **1**(2), 100021 (2022)
4. H. Liu, L. Wang, S. Wei, Y. Wu, Y. Zheng, F. Yuan, J. Hou, Study on photocatalytic degradation of amoxicillin in wastewater by Bi_2WO_6/nano-ZnO. Opt. Mater. **123**, 111835 (2022)
5. N. Kovalevskiy, S. Cherepanova, E. Gerasimov, M. Lyulyukin, M. Solovyeva, I. Prosvirin, D. Kozlov, D. Selishchev, Enhanced photocatalytic activity and stability of Bi(2)WO(6)–TiO(2)-N nanocomposites in the oxidation of volatile pollutants. Nanomaterials (Basel) **12**(3), 359 (2022)
6. S. Dong, X. Ding, T. Guo, X. Yue, X. Han, J. Sun, Self-assembled hollow sphere shaped Bi_2WO_6/RGO composites for efficient sunlight-driven photocatalytic degradation of organic pollutants. Chem. Eng. J. **316**, 778–789 (2017)
7. S. Li, C. Wang, M. Cai, Y. Liu, K. Dong, J. Zhang, Designing oxygen vacancy mediated bismuth molybdate (Bi_2MoO_6)/N-rich carbon nitride (C3N5) S-scheme heterojunctions for boosted photocatalytic removal of tetracycline antibiotic and Cr(VI): Intermediate toxicity and mechanism insight. J. Colloid Interface Sci. **624**, 219–232 (2022)
8. S. Li, M. Cai, C. Wang, Y. Liu, N. Li, P. Zhang, X. Li, Rationally designed Ta3N5/BiOCl S-scheme heterojunction with oxygen vacancies for elimination of tetracycline antibiotic and Cr(VI): Performance, toxicity evaluation and mechanism insight. J. Mater. Sci. Technol. **123**, 177–190 (2022)
9. M. Cai, C. Wang, Y. Liu, R. Yan, S. Li, Boosted photocatalytic antibiotic degradation performance of $Cd_{0.5}Zn_{0.5}S$/carbon dots/Bi_2WO_6 S-scheme heterojunction with carbon dots as the electron bridge. Sep. Purif. Technol. **300**, 121892 (2022)
10. S. Li, C. Wang, Y. Liu, B. Xue, W. Jiang, Y. Liu, L. Mo, X. Chen, Photocatalytic degradation of antibiotics using a novel Ag/Ag_2S/Bi_2MoO_6 plasmonic p-n heterojunction photocatalyst: Mineralization activity, degradation pathways and boosted charge separation mechanism. Chem. Eng. J. **415**, 128991 (2021)
11. S. Li, M. Cai, Y. Liu, J. Zhang, C. Wang, S. Zang, Y. Li, P. Zhang, X. Li, In situ construction of a C_3N_5 nanosheet/Bi_2WO_6 nanodot S-scheme heterojunction with enhanced structural defects for the efficient photocatalytic removal of tetracycline and Cr(vi). Inorg. Chem. Front. **9**(11), 2479–2497 (2022)
12. S. Li, M. Cai, Y. Liu, C. Wang, R. Yan, X. Chen, Constructing $Cd_{0.5}Zn_{0.5}S$/Bi_2WO_6 S-scheme heterojunction for boosted photocatalytic antibiotic oxidation and Cr(VI) reduction. Adv. Powder Mater. **2**(1), 100073 (2022)
13. Y. Huang, X. Zhang, Z. Zhou, S. Shen, A new and facile co-modification by introducing oxygen vacancies and loading Ag nanoparticles to promote the photocatalytic activities of Bi_2WO_6. Mater. Res. Bull. **119**, 110538 (2019)
14. J. Wang, L. Tang, G. Zeng, Y. Deng, H. Dong, Y. Liu, L. Wang, B. Peng, C. Zhang, F. Chen, 0D/2D interface engineering of carbon quantum dots modified Bi_2WO_6 ultrathin nanosheets with enhanced photoactivity for full spectrum light utilization and mechanism insight. Appl. Catal. B **222**, 115–123 (2018)
15. Y. Pan, X. Yuan, L. Jiang, H. Wang, H. Yu, J. Zhang, Stable self-assembly AgI/UiO-66(NH2) heterojunction as efficient visible-light responsive photocatalyst for tetracycline degradation and mechanism insight. Chem. Eng. J. **384**, 123310 (2020)
16. M. Bonneau, C. Lavenn, P. Ginet, K.-I. Otake, S. Kitagawa, Upscale synthesis of a binary pillared layered MOF for hydrocarbon gas storage and separation. Green Chem. **22**(3), 718–724 (2020)
17. M.I. Hossain, T.G. Glover, Kinetics of water adsorption in UiO-66 MOF. Ind. Eng. Chem. Res. **58**(24), 10550–10558 (2019)
18. G.-L. Yang, X.-L. Jiang, H. Xu, B. Zhao, Applications of MOFs as luminescent sensors for environmental pollutants. Small **17**(22), 2005327 (2021)
19. A. Ahmad, S. Khan, S. Tariq, R. Luque, F. Verpoort, Self-sacrifice MOFs for heterogeneous catalysis: synthesis mechanisms and future perspectives. Mater. Today **55**, 137 (2022)
20. Y. Xue, Y. Ji, X. Wang, H. Wang, X. Chen, X. Zhang, J. Tian, Heterostructuring noble-metal-free 1T' phase MoS_2 with g-C_3N_4 hollow nanocages to improve the photocatalytic H_2 evolution activity. Green Energy Environ. (2021). https://doi.org/10.1016/j.gee.2021.11.002
21. X. Wang, Y. Xue, Z. Liang, J. Tian, X. Zhang, X. Chen, Insights into the function of semi-metallic 1T' phase ReS_2 as cocatalyst decorated g-C_3N_4 nanotubes for enhanced photocatalytic hydrogen production activity. Mater. Today Adv. **15**, 100257 (2022)
22. Q. Zhao, J. Wang, Z. Li, Y. Guo, J. Wang, B. Tang, Y. Kansha, A. Yoshida, A. Abudula, G. Guan, UiO-66-NH2/Cu_2O composite as an enhanced visible light photocatalyst for decomposition of organic pollutants. J. Photochem. Photobiol. A **399**, 112625 (2020)
23. S. Wan, M. Ou, Q. Zhong, X. Wang, Perovskite-type CsPbBr 3 quantum dots/UiO-66(NH2) nanojunction as efficient visible-light-driven photocatalyst for CO_2 reduction. Chem. Eng. J. **358**, 1287–1295 (2019)

24. Y. Tan, Y. Zhou, Y. Deng, H. Tang, H. Zou, Y. Xu, J. Li, A novel UiO-66-NH2/Bi_2WO_6 composite with enhanced pollutant photodegradation through interface charge transfer. Colloids Surf. A **622**, 126699 (2021)
25. K. Jin, M. Qin, X. Li, R. Wang, Y. Zhao, Y. Li, H. Wang, A low-dosage silver-loaded flower-like Bi_2WO_6 nanosheets toward efficiently photocatalytic degradation of sulfamethoxazole. Mater. Sci. Semicond. Process. **139**, 106338 (2022)
26. K. Xu, J. Shen, S. Zhang, D. Xu, X. Chen, Efficient interfacial charge transfer of BiOCl-In_2O_3 step-scheme heterojunction for boosted photocatalytic degradation of ciprofloxacin. J. Mater. Sci. Technol. **121**, 236–244 (2022)
27. J. Di, C. Chen, C. Zhu, M. Ji, J. Xia, C. Yan, W. Hao, S. Li, H. Li, Z. Liu, Bismuth vacancy mediated single unit cell Bi_2WO_6 nanosheets for boosting photocatalytic oxygen evolution. Appl. Catal. B **238**, 119–125 (2018)
28. S. Li, J. Chen, S. Hu, H. Wang, W. Jiang, X. Chen, Facile construction of novel Bi_2WO_6/Ta3N5 Z-scheme heterojunction nanofibers for efficient degradation of harmful pharmaceutical pollutants. Chem. Eng. J. **402**, 126165 (2020)
29. X. Zhang, H. Zhou, W. Cao, C. Chen, C. Jiang, Y. Wang, Preparation and mechanism investigation of Bi_2WO_6/UiO-66-NH2 Z-scheme heterojunction with enhanced visible light catalytic activity. Inorg. Chem. Commun. **120**, 108162 (2020)
30. R. Liu, S. Meng, Y. Ma, L. Niu, S. He, X. Xu, B. Su, D. Lu, Z. Yang, Z. Lei, Atmospherical oxidative coupling of amines by UiO-66-NH2 photocatalysis under milder reaction conditions. Catal. Commun. **124**, 108–112 (2019)
31. X. Zhang, M. Liu, R. Han, Adsorption of phosphate on UiO-66-NH2 prepared by a green synthesis method. J. Environ. Chem. Eng. **9**(6), 106672 (2021)
32. C. Zhao, A. Zhou, Y. Dou, J. Zhou, J. Bai, J.-R. Li, Dual MOFs template-directed fabrication of hollow-structured heterojunction photocatalysts for efficient CO_2 reduction. Chem. Eng. J. **416**, 129155 (2021)
33. T. Qian, Y. Zhang, J. Cai, W. Cao, T. Liu, Z. Chen, J. Liu, F. Li, L. Zhang, Decoration of amine functionalized zirconium metal organic framework/silver iodide heterojunction on carbon fiber cloth as a filter- membrane-shaped photocatalyst for degrading antibiotics. J. Colloid Interface Sci. **603**, 582–593 (2021)
34. S.H. Paiman, M.A. Rahman, T. Uchikoshi, N. Abdullah, M.H.D. Othman, J. Jaafar, K.H. Abas, A.F. Ismail, Functionalization effect of Fe-type MOF for methylene blue adsorption. J. Saudi Chem. Soc. **24**(11), 896–905 (2020)
35. Y. Qiu, J. Lu, Y. Yan, J. Niu, Enhanced visible-light-driven photocatalytic degradation of tetracycline by 16% Er3+-Bi_2WO_6 photocatalyst. J. Hazard. Mater. **422**, 126920 (2022)
36. M. Peñas-Garzón, M.J. Sampaio, Y.L. Wang, J. Bedia, J.J. Rodriguez, C. Belver, C.G. Silva, J.L. Faria, Solar photocatalytic degradation of parabens using UiO-66-NH2. Sep. Purif. Technol. **286**, 120467 (2022)
37. K. Zhang, J. Wang, W. Jiang, W. Yao, H. Yang, Y. Zhu, Self-assembled perylene diimide based supramolecular heterojunction with Bi_2WO_6 for efficient visible-light-driven photocatalysis. Appl. Catal. B **232**, 175–181 (2018)
38. B. Li, C. Lai, G. Zeng, L. Qin, H. Yi, D. Huang, C. Zhou, X. Liu, M. Cheng, P. Xu, C. Zhang, F. Huang, S. Liu, Facile hydrothermal synthesis of Z-scheme Bi(2)Fe(4)O(9)/Bi(2)WO(6) heterojunction photocatalyst with enhanced visible light photocatalytic activity. ACS Appl. Mater. Interfaces **10**(22), 18824–18836 (2018)
39. J. Wang, W. Lin, M. Dong, Y. Xing, Q. Zhang, Facile synthesize of CdS QDs decorated Bi(2)MoO(6)/Bi(2)Mo(3)O(12) heterojunction photocatalysts and enhanced performance of visible light removal of organic pollutants. Environ. Technol. **42**(23), 3581–3594 (2021)
40. Z. Ding, M. Sun, W. Liu, W. Sun, X. Meng, Y. Zheng, Ultrasonically synthesized N-TiO_2/Ti_3C_2 composites: enhancing sonophotocatalytic activity for pollutant degradation and nitrogen fixation. Sep. Purif. Technol. **276**, 119287 (2021)
41. Q. Yang, W. Lin, Z. Duan, S. Xu, J. Chen, X. Mai, Bismuth-doped g-C(3)N(4)/ZIF-8 heterojunction photocatalysts with enhanced photocatalytic performance under visible light illumination. Environ. Technol. (2021). https://doi.org/10.1080/09593330.2021.1996467
42. D. Huang, J. Li, G. Zeng, W. Xue, S. Chen, Z. Li, R. Deng, Y. Yang, M. Cheng, Facile construction of hierarchical flower-like Z-scheme AgBr/Bi_2WO_6 photocatalysts for effective removal of tetracycline: degradation pathways and mechanism. Chem. Eng. J. **375**, 121991 (2019)
43. R. Atla, T.H. Oh, Novel fabrication of the recyclable MoS_2/Bi_2WO_6 heterostructure and its effective photocatalytic degradation of tetracycline under visible light irradiation. Chemosphere **303**, 134922 (2022)
44. T. Yao, Y. Tan, Y. Zhou, Y. Chen, M. Xiang, Preparation of core-shell MOF-5/Bi_2WO_6 composite for the enhanced photocatalytic degradation of pollutants. J. Solid State Chem. **308**, 122882 (2022)
45. H. Yi, M. Yan, D. Huang, G. Zeng, C. Lai, M. Li, X. Huo, L. Qin, S. Liu, X. Liu, B. Li, H. Wang, M. Shen, Y. Fu, X. Guo, Synergistic effect of artificial enzyme and 2D nano-structured Bi_2WO_6 for eco-friendly and efficient biomimetic photocatalysis. Appl. Catal. B **250**, 52–62 (2019)
46. Q. Zhang, Q. Yang, S. Xu, Z. Duan, W. Lin, Enhanced visible-light photocatalytic activity by Ag3PO4–Ag–Bi2WO6 Z-scheme heterojunction. Micro Nano Lett. **15**(14), 1055–1058 (2020)